How can existing ground-based profiling instruments improve European weather forecasts?

Article

Accepted Version

It is advisable to refer to the publisher's version if you intend to cite from the work. See Guidance on citing.

To link to this article DOI: http://dx.doi.org/10.1175/BAMS-D-17-0231.1

www.reading.ac.uk/centaur

EARLY ONLINE RELEASE

This is a preliminary PDF of the author-produced manuscript that has been peer-reviewed and accepted for publication. Since it is being posted so soon after acceptance, it has not yet been copyedited, formatted, or processed by AMS Publications. This preliminary version of the manuscript may be downloaded, distributed, and cited, but please be aware that there will be visual differences and possibly some content differences between this version and the final published version.

1   How can Existing Ground-Based Profiling Instruments

2   Improve European Weather Forecasts?

3

4   Authors:

5   A. J. Illingworth[*1], D. Cimini[2], A. Haefele[3], M. Haeffelin[4], M. Hervo[3], S. Kotthaus[4], U.

6   Löhnert[5], P. Martinet[6], I. Mattis[7], E. J. O'Connor[8], and R. Potthast[9]

7

8   Affiliations:

9   [1]Department of Meteorology, University of Reading, UK

10   [2]CNR-IMAA, Potenza, Italy & CETEMPS, University of L'Aquila, Italy

11   [3]MeteoSwiss, Payerne, Switzerland

12   [4]Institut Pierre Simon Laplace, Ecole Polytechnique, Palaiseau, France

13   [5]Institute for Geophysics and Meteorology, University of Cologne, Germany

14   [6]CNRM UMR 3589, Meteo France/CNRS, Toulouse, France

15   [7]Deutscher Wetterdienst, Observatorium Hohenpeißenberg, Germany

16   [8]Finnish Meteorological Institute, Finland

17   [9]Deutscher Wetterdienst, Offenbach, Germany

18

19   * *Corresponding author address*: Anthony J. Illingworth, Department of Meteorology,

20   University of Reading, Earley Gate, PO Box 243, Reading RG6 6BB, UK

21   Tel: +44 118 378 6508   E-mail: a.j.illingworth@reading.ac.uk

22

23   ABSTRACT

24   To realise the promise of improved predictions of hazardous weather such as flash floods, wind

25   storms, fog and poor air quality from high-resolution mesoscale models, the forecast models

26 must be initialized with an accurate representation of the current state of the atmosphere, but

27 the lowest few km are hardly accessible by satellite, especially in dynamically-active

28 conditions. We report on recent European developments in the exploitation of existing ground-

29 based profiling instruments so that they are networked and able to send data in real-time to

30 forecast centers. The three classes of instruments are: (i) Automatic lidars and ceilometers

31 providing backscatter profiles of clouds, aerosols, dust, fog and volcanic ash, the last two being

32 especially important for air traffic control; (ii) Doppler wind lidars deriving profiles of wind,

33 turbulence, wind shear, wind-gusts and low-level jets; and (iii) Microwave radiometers

34 estimating profiles of temperature and humidity in nearly all weather conditions. Twenty-two

35 European countries and fifteen European National Weather Services are collaborating in the

36 project, that involves the implementation of common operating procedures, instrument

37 calibrations, data formats and retrieval algorithms. Currently, data from 220 ceilometers in 17

38 countries are being distributed in near real-time to national weather forecast centers; this should

39 soon rise to many hundreds. The wind lidars should start delivering real time data in late 2018,

40 and the plan is to incorporate the microwave radiometers in 2019. Initial data assimilation tests

41 indicate a positive impact of the new data.

42

43 CAPSULE

44 Observations of profiles of winds, aerosol, clouds, winds, temperature and humidity in the

45 lowest few km of the atmosphere from networks of ceilometers, Doppler wind lidars and

46 microwave radiometers are starting to flow in real time to forecasting centers in Europe.

47

48 The high-resolution (1 km) forecasting models that are now run operationally by many

49 European National Weather Services promise to provide increasingly accurate high-resolution

50 forecasts of impending hazardous weather, ranging from flash floods to episodes of poor air

51 quality. The WMO guidance for NWP applications highlights the need for wind, temperature

52 and humidity profiles, especially in cloudy areas[1]. Satellites can provide data in the upper

53 troposphere, but if this promise is to be fulfilled, in particular for short-range forecasts, a new

54 generation of high-density observations through the lower few km of the atmosphere, including

55 the boundary layer, is required in real-time. This region close to the ground is particularly

56 difficult to observe with satellites due to the frequent occurrence of clouds and, for passive

57 instruments, the broad weighting functions and the effects of the variable albedo or brightness

58 temperature of the surface.

59

60 Illingworth et al. (2015) noted the potential of ground-based networks of automatic low-power

61 backscatter lidars/ceilometers (ALC)[2], Doppler Wind Lidars (DWL) and Microwave

62 Radiometers (MWR) to supply real-time observation to forecast centers. In this paper we report

63 recent developments in the exploitation of these networks. Observations of profiles of aerosols,

64 clouds, winds, temperature and humidity in the lowest few km of the atmosphere in Europe are

65 now starting to flow in real time to forecasting centers. This has been achieved as a result of

66 collaboration between a COST action (see sidebar) 'TOPROF: Towards operational ground-

67 based profiling with ALCs, DWL and MWRs for improving weather forecasts'

68 (www.cost.eu/COST_Actions/essem/ES1303) and EUMETNET, an organization which

69 provides a framework to enable the European Weather Services to work together, share ideas,

70 best practice and to share the cost of major infrastructure investments. The EUMETNET

71 Composite Observing System (EUCOS) is responsible for developing an observing system for

---

[1] See WMO statements of guidance for high-resolution and global NWP at:
https://www.wmo.int/pages/prog/www/OSY/SOG/SoG-HighRes-NWP.pdf
https://www.wmo.int/pages/prog/www/OSY/SOG/SoG-Global-NWP.pdf
[2] Ceilometers were originally conceived to measure cloud base altitude only, but today the sensitivity of these instruments is sufficient to provide profiles of backscattered power from aerosols and clouds. Hence a new terminology has been proposed that combines automatic low-power lidars and ceilometers into ALCs.

72 Europe serving the needs of regional numerical weather prediction (NWP). One of

73 EUMETNET's programs is 'E-PROFILE' that originally involved only radar wind profilers,

74 but has been extended to include ALC networks and more recently is incorporating DWLs with

75 a projected extension to distribute MWR data. The TOPROF action ran from October 2013 to

76 October 2017 with financial support from the European Union and was responsible for setting

77 up common calibration techniques, operating procedures, deriving error characteristics,

78 developing retrieval algorithms, and ensuring homogeneous and reliable data quality for the

79 three classes of instruments, whereas EUMETNET through its E-PROFILE program is

80 involved in the networking and near real-time distribution of observations to the national

81 weather services.

82

83 The ALCs under investigation in the E-PROFILE network transmit short pulses of laser

84 radiation with wavelengths 532, ~ 910 or 1064 nm and receive a backscattered signal with a

85 delay that provides range information. The raw data are averaged to 15-30m vertical resolution

86 and 15-60 seconds in time. Examples of the use of attenuated backscatter profiles include

87 characterising clouds, aerosols, dust, fog and volcanic ash as discussed in more detail in the

88 ALC section, the last two being especially important for air traffic control. At present,

89 attenuated backscatter profiles from over 220 ALCs in 17 countries are being distributed by

90 EUMETNET E-PROFILE in near real-time to National Weather Services and can be viewed

91 at http://eumetnet.eu/e-profile/, (Wiegner et al. 2014). These data are homogenized and

92 calibrated using the developments carried out in TOPROF.

93

94 Fig. 1 represents the map of E-PROFILE stations in green and stations that will be integrated

95 before the end of 2018 in blue: ALCs that are present in Europe but not yet integrated into E-

96 PROFILE are in red (data from DWDs ceilomap https://www.dwd.de/ceilomap). In June 2018,

97　the Saddleworth Moor fire near Manchester injected large quantities of smoke into the

98　atmosphere. This smoke was transported over UK and Europe and measured by the E-

99　PROFILE network. The measurements from 26 to 28 June at five E-PROFILE stations are

100　displayed in Fig. 1. Aerosol layers are visible in the free troposphere (at altitudes between 2

101　and 5 km). Measurements above thick clouds (represented with black dots) appear as white

102　vertical stripes because the laser beam is fully attenuated. These measurements are also visible

103　on the E-PROFILE website and clearly illustrate the capabilities of the network in monitoring

104　aerosol layers over Europe.

105

106　In contrast to ALCs which have been in use for many years, DWLs have undergone recent

107　development using solid-state fibre-optic technology at a wavelength of ~1.5 μm. The type of

108　DWL being incorporated into the E-PROFILE network obtains the radial Doppler shift of the

109　backscattered signal from aerosol or cloud particles in the direction of the beam using the high

110　pulse rate heterodyne technique. From the radial Doppler velocities, the vertical structure of

111　winds, wind shear, levels of turbulence, inference of the maximum gusts, properties of low-

112　level jets and classification of the state of the boundary layer can be obtained.　The minimum

113　range is typically 50-90 m, with the maximum range varying from 2-10 km; in practice the

114　sensitivity of most instruments usually limits the observations to within the boundary layer

115　where there are sufficient aerosols. Wind measurements are not possible inside or above

116　optically thick clouds or in heavy rain.

117

118　Ground-based microwave radiometers (MWR) measure the natural down-welling thermal

119　emission in the microwave part of the electromagnetic spectrum originating from Earth's

120　atmosphere and the cosmic background. The radiance observations are commonly expressed

121　as an equivalent brightness temperature (T_B) from which estimates of atmospheric temperature

122   profiles (from oxygen absorption from 55 to 60 GHz) and humidity profiles (from water vapor

123   absorption around 22 GHz) as well as column-integrated water vapor (IWV) and liquid water

124   path (LWP) can be inferred during non-precipitating conditions. Valid temperature profiles can

125   also be inferred in the presence of low-moderate precipitation. The MWR profiling capability

126   in the lowest 2 km of the atmosphere is proving to be valuable because of the poor sampling

127   by other sensors (e.g. from satellite).

128

129   All these instruments are rugged and can operate autonomously for long periods requiring little

130   maintenance and do not need specialised staff, but how can these new observations contribute

131   to NWP? Firstly, they can be used to check that the parameterisation schemes inherent in such

132   models lead to a realistic representation of the current state of the atmosphere. For more than

133   ten years the Cloudnet project (Illingworth et al. 2007) has used vertically pointing cloud

134   radars, ACLs and MWRs to derive cloud properties, compared them with the representation of

135   clouds within several operational European forecast models and produced statistics of the

136   model performance (http://cloudnet.fmi.fi). In Cloudnet the ALCs were only used to identify

137   cloud base of liquid clouds and the MWRs to derive their liquid water path. A more rigorous

138   approach is to compare the observations ('O') with their representation in the model (the

139   background 'B') to obtain the 'O-B' statistics and to check that any biases are sufficiently small

140   and, ideally, that the errors are Gaussian. This procedure is fairly straightforward for the winds

141   from a DWL because the model has a prognostic wind variable. This is not the case for the

142   ALC backscatter signal nor for the brightness temperature from microwave radiometers, so a

143   *'forward model'* must be used that operates on the prognostic variables within the NWP model

144   to predict the value of the observed parameter which can then be directly compared with the

145   observation. Once the O-B statistics are deemed to be acceptable then there is potential for

146   *data assimilation* whereby the initial state of the model is updated with the observations

147   accounting for the errors in both the observations and the model, so that the NWP model can

148   be initialised with the best possible representation of the current state of the atmosphere. A

149   more accurate initial state usually reduces the errors in the forecast.

150

151   If the new observations are to be useful, then it is essential that the data are calibrated and

152   unbiased and the quality is homogeneous with known error characteristics. TOPROF's major

153   tasks have been to establish common calibration procedures for the three classes of instruments,

154   common checks on data quality, and independent validation of the veracity of the data.

155   TOPROF has also developed forward models for predicting the ALC and MWR observations

156   from the NWP representation, and defined common data formats and protocols for transmitting

157   the data to a central hub from where they can be distributed to the national weather services.

158   Finally, TOPROF has started gathering O-B statistics of model performance and carried out

159   some simple data assimilation trials that indicate a positive impact on the forecast.

160

161   **AUTOMATIC LOW-POWER LIDARS AND CEILOMETERS (ALCS).**

162   Figure 2 shows a warm front crossing Germany in the morning of 25 August 2018 as observed

163   at Ulm by a CHM15-k ceilometer of the DWD network. The cloud base height descended from

164   10 km at midnight to 2.5 km at 0800 UTC. Rain started at 0900 UTC, visible as red vertical

165   stripes between the cloud base and the ground. The yellowish horizontal line at 2 km altitude

166   between 1200 and 1500 UTC shows the melting layer (dark band). After the frontal passage

167   (at about 1500 UTC), the steady rain stopped and the stratiform clouds were replaced by broken

168   cumulus, with some precipitation below cloud base that occasionally reached the ground.

169   Liquid water clouds can be identified by a thin layer with very high backscatter at cloud base

170   followed by rapid extinction of the ceilometer signal, for example near heights of 2-3 km at

171   0000, 0200 and from 1700 - 2100 UTC, whereas the ceilometer signal penetrates further into

ice clouds. Before the frontal passage the planetary boundary layer (PBL) was characterized by a significant aerosol load with backscatter values > 1 Mm^{-1} sr^{-1} up to ~2 km height, but was cleaner during the afternoon; this could be due to wash-out or a different, cleaner air mass. Note the two thin aerosol layers from long range transport (in yellow) at 8 and 10.5 km altitude after 2200 UTC with backscatter values ~ 0.5 Mm^{-1} sr^{-1}, possibly from forest fires in North America.

Three classes of ALCs are being used in the E-PROFILE network. CL31 and CL51 from Vaisala measuring at ~ 910 nm, CHM15k from Lufft measuring at 1064 nm and Mini-MPL from Sigma-Space, measuring at 532 nm. Other ALCs are also exploited at some sites such as, for example, the CS135 from Campbell Scientific (910 nm) or the CE370 from CIMEL (532 nm). ALCs are characterized by their continuous 24-7 operation capabilities with high sampling rates. In the low-altitude range, the optical overlap between the emitting (laser) and receiving (telescope) optical components of an ALC changes with altitude. If this overlap function is not well characterized, exploitation of the measurements at low-altitude may be restricted. In the far-altitude range, the signal-to-noise ratio may limit the exploitation of the measurements for detecting low-scattering media such as aerosols. Some more sensitive systems may, on the contrary, suffer from saturation due to high-scattering media such as liquid water clouds at short range. Some of these effects can be corrected to improve signal quality. All ALCs must also be calibrated in order to derive quantitatively meaningful attenuated backscatter profiles that can be compared from one instrument to the next and with values predicted from NWP forward models.

a*) Determining optical overlap functions.* The optical design of CL31 (CL51) instruments yield a complete overlap around 50m (200m) (e.g. Haeffelin et al. 2012; Wiegner et al. 2014). The bi-axial lidars like CHM15k or Mini-MPL reach complete optical overlap around 1km with

197 very noisy signal below 150-200 m, a region where the optical overlap is close to zero. Hervo

198 et al. (2016) found that the optical overlap function of the CHM15k is affected by temperature

199 fluctuations. They developed a methodology to determine the temperature dependence and

200 correct for it, yielding a precise attenuated backscatter values in the partial overlap region.

201 b) *Correcting signal artifacts*. Kotthaus et al. (2016) found signal artifacts in the free

202 troposphere in CL31 attenuated backscatter profiles, characterized by negative values in cloud-

203 free regions due to a shift of the raw data introduced by the system firmware, and developed a

204 method to quantify these artifacts and correct for them. These results convinced Vaisala to

205 release a new firmware for TOPROF that removes the artificial shifts to allow more

206 quantitative exploitation of the CL31 attenuated backscatter profiles;

207 c) *ALC Calibration*. The signal detected by the ceilometers must be converted into an absolute

208 value of backscatter measured in units of m^{-1} sr^{-1}. This is best accomplished by using a

209 reference target whose backscatter characteristics are known. One approach uses the known

210 integrated backscatter for a water cloud that total extinguishes the ceilometer signal; this can

211 be obtained by adding the observed backscatter at each gate within the cloud, and adjusting the

212 ceilometer calibration until this integral, after correction for multiple scattering, is equal to

213 0.027 m $^{-1}$. For details see O'Connor et al. (2004). Hopkins et al. (submitted to AMT) showed

214 that this calibration is accurate to better than 10% with no significant annual variation. A second

215 approach for photon-counting instruments measuring at 532 or, more commonly at 1064 nm,

216 is to use the molecular return as a reference because it is a function of the known air density

217 (Fernald et al. 1972; Klett, 1985; Wiegner and Geiß, 2012; Baars et al. 2016). The molecular

218 return at 1064 nm is small, but photon counting instruments are able to measure it with

219 sufficiently long averaging times (Wiegner and Geiß, 2012) and Fig. A2 in Baars et al. (2016).

220 The method developed within TOPROF relies on averaging the backscatter return for 6

221 hours on a clear night; sensitivity studies showed that typical accuracies of the calibration are

222   of the order of 10%-15%. The calibrations can be up to a factor of two different from those

223   supplied by the manufacturer. These two methods are implemented by E-PROFILE to

224   distribute calibrated attenuated backscatter data to national weather services. Wiegner and

225   Gasteiger (2015) propose a method to correct for water vapor absorption for ALC

226   measurements that operate at wavelengths affected by this effect (e.g. 905-910 nm).

227   d) *ALC measurement uncertainties for Lufft and Vaisala due to incomplete optical overlap,*

228   *signal artifacts, and calibration*. These have been estimated using data from a three-month

229   experiment 'CEILINEX' when 12 ALCs were operated side-by-side (https://ceilinex2015.de/,

230   Pattantyús-Ábrahám et al. 2017). Fig. 3 shows a comparison of raw ALC signal and calibrated

231   attenuated backscatter signal from 8 co-located ALCs including Campbell Scientific, Vaisala,

232   and Lufft instruments based on 3 hours of data on 13 Aug 2015. The profiles show a stable

233   nocturnal boundary layer up to 300 m and a residual layer up to 750 m. Additionally, there are

234   two lofted aerosol layers (probably Saharan dust) between 1 and 4 km. Fig. 3 shows that

235   differences less than 25% can be expected for calibrated attenuated backscatter, in particular

236   for altitudes greater than 500 m. Below 500 m the greater differences between the Lufft and

237   Vaisala instruments can be attributed to systematic errors in the overlap function correction.

238   Note also inconsistencies below 250 m between CL31 and CL51 profiles and between the

239   different Lufft ALCs, confirming that data should be used with great care at such low altitudes.

240   CL31 and CL51 measurements have a lower signal-to-noise ratio than the other instruments at

241   altitudes greater than 1000 m and so are less sensitive for monitoring lofted aerosol.

242

243   Applications using ALC measurements are numerous. Several studies were conducted in the

244   framework of the TOPROF action that resulted in the evaluation of aerosols in atmospheric

245   models based on ALC forward models and O-B statistics (e.g. Warren et al. 2018), providing

246   diagnostics of the atmospheric boundary layer height (Lotteraner and Piringer 2016; Poltera et

247   al. 2017; Kotthaus and Grimmond, 2018), supporting warning of fog formation (Haaeffelin et

248   al. 2016), and detecting transport of dust, biomass burning and volcanic ash (Cazorla et al.

249   2017; Roman et al. 2018). Fig. 4 shows an example of comparisons between attenuated

250   backscatter observed by an ALC and modeled using the ECMWF CAMS forward model[3]. The

251   observations were performed by a CHM15k in Valladolid and calibrated using the

252   methodology described above. Saharan dust aerosols are clearly visible up to 5 km, both in the

253   observations and the forecasts. The mean bias for this event is lower than 5%, showing the

254   good agreement between observations and forecasts. Chan et al. (2018) carried out a year- long

255   comparison of the representation of aerosols within the CAMS model and from the German

256   ceilometer network and found very good agreement with the arrival time and vertical extent of

257   a Saharan dust layer. Fig. 5 shows an example of low-altitude ALC-derived information during

258   3 hours in pre-fog conditions at the Charles-de-Gaulle airport near Paris. The bottom panel

259   shows the 0-400 m ALC attenuated backscatter profile, while the top panel provides fog alerts

260   based on Haeffelin et al. (2016). At 0430h, more than 1 hour before the first alerts, the sky is

261   cloud free (bottom panel) favoring radiative cooling and the ALC backscatter is quite high

262   between 50-150 m, revealing the presence of large aerosols in a moist atmosphere. At 0550h,

263   a cloud forms about 100 m agl generating severe-level alerts aloft, and rapidly subsides to the

264   ground, leading to persistent fog after 0645h, about 1 hour after the first severe-level alerts.

265

266   **DOPPLER WIND LIDARS (DWLs)**

267   The Doppler lidar instruments considered by the TOPROF action were those with sufficient

268   sensitivity and a scanning capability so that the horizontal wind profile could be derived

269   throughout the boundary layer. These included instruments from Halo Photonics (Streamline,

---

[3] Developed for the CALIOP lidar data from CALIPSO satellite in the A-train, (Benedetti et al., 2009) but looking upwards instead of downwards. The model carries aerosol type and size and so the optical depth/extinction is calculated, and the assumed lidar ratio converts extinction into the observed value of backscatter.

270   Streamline Pro and Streamline XR) and Leosphere (WindCube 100S, 200S and 400S), all

271   configurable to have a maximum range of about 10 km and range resolution of 50 m or better.

272   All DWL considered in TOPROF are full-hemispheric scanning, except for the Halo Photonics

273   Streamline Pro, which can scan within a cone from 70° above the horizon to zenith and has no

274   external moving parts. One task in TOPROF was to design suitable scanning strategies

275   optimized to extract as much information as possible. The scanning capability is utilized to

276   reconstruct the vertical profile of the horizontal wind from the measured radial components.

277   This can be performed in a similar manner as for radar wind profilers by means of 'Doppler

278   Beam Swinging' where the wind speed and direction are derived from the radial (line-of-sight)

279   components from off-zenith dwells at different azimuths, or by using a conical Velocity-

280   Azimuth-Display (VAD) scan where the wind speed and direction can be inferred from the

281   magnitude and phase of the sinusoidal azimuthal variation of the observed radial component

282   of the wind. Both methods rely on assuming horizontal homogeneity in order to derive the

283   horizontal component; this may not be applicable in strongly turbulent situations, or in flows

284   over complex terrain. TOPROF recommends performing a VAD scan with a minimum of 12

285   beams, and, using the method of Päschke et al. (2015), which, in addition to generating the

286   horizontal wind profile, provides a metric describing the likelihood of inhomogeneity

287   degrading the retrieval. Teschke and Lehmann (2017) note that the optimal elevation angle for

288   a VAD scan is about 35° from horizontal but that this is not a strong constraint; suitable

289   elevation angles for VAD scanning lie between 15 and 70° from horizontal. Hence, TOPOROF

290   recommends performing two VAD scans; a primary scan at high elevation (50-70° from

291   horizontal) to capture the wind profile to the top of the boundary layer; and a rapid low-

292   elevation scan at 15° or lower in elevation (dependent on local obstructions), from which the

293   vertical profile can be extended down towards the surface below the minimum altitude probed

294   by the higher elevation scan. The inclusion of an additional scan at a low elevation can also be

295   used to investigate the spatial representativeness of the wind profile.

296

297   Such high vertical resolution wind profiles are ideal for capturing the presence of wind shear,

298   and low-level jets, an important consideration for wind energy, aviation, and air quality

299   applications. An objective method for diagnosing low-level jets was developed (Tuononen et

300   al., 2017) and is now being implemented routinely at a number of sites (Marke et al., 2018).

301   Vertical dwells with high temporal resolution (5 seconds or better) within the VAD scans allow

302   the retrieval of turbulent parameters such as vertical velocity variance, skewness and

303   dissipation rate of turbulent kinetic energy (O'Connor et al., 2010). Combining these

304   parameters permits a classification of the atmospheric boundary layer structure (Manninen et

305   al, 2018) in which the turbulent regions are detected, and a probable source of turbulence

306   assigned: e.g. whether wind shear or buoyancy production dominates, or whether convection

307   is surface-driven or cloud-driven. The classification scheme also notes whether the turbulent

308   layers are in contact with the surface, an important distinction when calculating dispersion in

309   chemical transport models. Turbulent parameters can also be derived from VAD scans

310   (Vakkari et al., 2015), reconstructed using a stochastic particle filter (Rottner et al., 2017), and

311   the combination of winds and turbulence can be used to diagnose wind gusts (Suomi et al.,

312   2017) especially important in forecasting and assessing wind-induced damage.

313

314   DWL products can be used to validate the boundary layer schemes employed in forecast

315   models, even in challenging locations (a coastal example is given in Fig. 6), and to evaluate

316   the much more spatially dense ALC retrievals (Schween et al. 2014). Generating these new

317   products routinely requires that DWL uncertainties are known and well characterized. Known

318   hard targets such as towers and masts can be used to check the radial Doppler velocity, and that

319   the pointing angle is correct. Azimuthal pointing repeatability for these instruments was shown

320   to be excellent, typically within 0.25°. Uncertainties in radial Doppler velocity estimates are a

321   function of the number of pulses sampled and their signal-to-noise ratio (SNR). TOPROF

322   worked together with the manufacturers on understanding and improving the data processing

323   to yield reliable data. Reducing the median bias in SNR to about 0.0002 led to improvements

324   in sensitivity by as much as a factor of 5 to 10 (Manninen et al. 2016), so that a lower SNR

325   threshold could be used to diagnose 'good' data. The bias reduction permits more reliable

326   uncertainty estimates, yielding more accurate turbulent parameters. Long-term comparisons of

327   the resulting wind estimates compare very well with masts and other measurements at high

328   SNR with root mean squared errors, RMSE, of < 0.7 m s^{-1} for wind speed and $< 10°$ for

329   direction (e.g. Päschke et al. 2015), but care should be taken when calculating wind

330   climatologies in low SNR conditions (Gryning et al. 2016). Now that the data quality has been

331   established the next step is a to establish the O-B statistics. In principle, DWLs provide profiles

332   of attenuated backscatter similar to ALCs. DWLs operating with a telescope focused at infinity

333   can use the same liquid cloud method as for ALCs (Westbrook et al. 2010) for calibrating the

334   backscatter power. However, by adjusting the telescope focus, extra sensitivity in the BL can

335   be achieved while sacrificing sensitivity in the far range; beneficial for retrieving winds and

336   turbulence in the boundary layer, but more difficult to account for in calculating the profile of

337   attenuated backscatter. Extensive comparisons with instrumented towers confirm the accuracy

338   of the winds derived from DWLs and a more comprehensive O-B comparison is planned using

339   the two-year data set obtained from the DWL network.

340

341

342   **MICROWAVE RADIOMETERS (MWRs)**

343   MWR measure downwelling radiation in terms of atmospheric brightness temperatures (T_B)

344   that are then converted to atmospheric variables of interest. TOPROF fostered breakthrough

345   developments in both MWR hardware and software leading to more accurate T_B observations,

346   relevant for direct data assimilation, and also to improved retrievals of atmospheric variables.

347   The instruments considered here are multi-channel temperature and humidity profilers

348   operating in the 22-31 (humidity) and 51-60 (temperature) GHz bands, such as Radiometer

349   Physics (RPG)[4] HATPRO and Radiometrics MP3000[5] (Ware et al. 2003; Rose et al. 2005; De

350   Angelis et al. 2017). These instruments also provide the column-integrated amount of water

351   vapor (IWV) and cloud liquid water path (LWP).

352

353   Two Joint Calibration (JCAL) field experiments were organized in cooperation with leading

354   MWR manufacturers, triggering the development of new calibration targets and receiver

355   technology. RPG has developed a new arrangement for the liquid nitrogen calibration target

356   that eliminates calibration uncertainties due to reflections and standing waves and provides

357   absolute accuracies of T_B on the order of 0.1 K, which is a factor ~5 more accurate than

358   previous targets. The load was introduced with the 5th HATPRO generation, which also

359   includes an improved receiver technology resulting in T_B noise levels also on the order of 0.1

360   K at 1 s temporal resolution. Czekala (personal communication) has shown that this can lead

361   to an uncertainty reduction of the temperature profile retrieval by up to 0.3 K, leading to more

362   reliable detection of temperature inversions in the boundary layer. These hardware

363   developments can also improve the accuracy of IWV and LWP retrievals by up to 50%. The

364   new calibration load is also compatible with radiometers of older generations.

365   Recommendations for operational calibration, measurement and quality procedures suited for

366   network operation were agreed upon and distributed

367   (http://cetemps.aquila.infn.it/mwrnet/reports.html). In addition, a software package for data

---

[4]https://www.radiometer-physics.de/products/microwave-remote-sensing-instruments/radiometers/humidity-and-temperature-profilers/

[5]http://radiometrics.com/mp-series/

368   post-processing including retrieval application, quick-look generation, and output conversion

369   (compliant with the Climate and Forecast metadata convention) for most common MWR types

370   is available (http://cetemps.aquila.infn.it/mwrnet/mwr_pro.html).

371

372   A fast forward model has been developed (De Angelis et al. 2016) by adapting existing

373   software widely used for satellite data assimilation so that it can calculate the downwelling T_{BS}

374   that would be observed at the ground and their Jacobians from any source of atmospheric

375   temperature and humidity profiles (e.g. radiosondes or an NWP model). The software,

376   RTTOV-gb, (http://cetemps.aquila.infn.it/mwrnet/rttovgb.html), is freely available, and

377   validation with a reference line-by-line (LBL) computation shows unbiased rms differences

378   within 0.2 K, so the error of the parametrized forward model is within the instrumental

379   uncertainty. In order to monitor the behavior of continuous T_B observations, O-B statistics were

380   computed for a 1-year dataset from a prototype network of six MWRs (De Angelis et al. 2017).

381   Within this network standardized calibrations procedures and data life cycle had been

382   implemented so that quality-controlled data were collected. The six prototype network stations

383   are located at: Cabauw, NL (51.97N/4.93E), Jülich, GER (50.91N/6.41E), Leipzig, GER

384   (51.35N/12.43E), Lindenberg, GER (52.21N/14.12E), Palaiseau, FRA (48.40N/2.36E), and

385   Payerne, SUI (46.82N/6.95E). Fig. 7 shows the 1-year time series of O-B comparison at one

386   site for four frequency channels. The NWP model used here is AROME, Application of

387   Research to Operations at Mesoscale, developed by Météo-France (Seity et al. 2011).

388

389   The O-B analysis revealed that typical differences are within the expected total uncertainty and

390   that the O-B distributions were Gaussian, confirming their suitability for variational data

391   assimilation.   The analysis also demonstrated how such monitoring is able to detect an

392   instrument malfunction leading to a mis-calibration and then to verify that a re-calibration has

393　been successful as described in Fig. 7. The O-B analysis showed consistent characteristics over

394　time and instrument site/type with a typical O-B bias for well-maintained instruments being

395　generally below 1K, but reaching ~3K at lower frequency oxygen channels, where the forward

396　model uncertainty reaches its maximum (De Angelis et al. 2017; Cimini et al. 2018). However,

397　even these uncertainties can be effectively addressed because the biases were persistent and the

398　random component was similar throughout the prototype network. The uncertainty of the

399　reference LBL calculations have also been investigated (Cimini et al. 2018), possibly

400　explaining systematic O-B differences exceeding 1 K that must be accounted for within a bias

401　correction scheme. A platform for continuously monitoring O-B quick-looks in near-real-time

402　is up and running and available for all interested users (https://tinyurl.com/MWR-O-B-

403　JOYCE). The main goal of this platform is i) to provide an independent instrument performance

404　monitoring tool for MWR operators and ii) to attest the suitability of MWR for operational use

405　by National Weather Services.

406

407　In addition to the prototype network, there are some 30 MWR stations over Europe that have

408　the potential to deliver T_Bs and derived products on a continuous basis. Details of the network

409　can be found at http://cetemps.aquila.infn.it/mwrnet/MWRnetmap.html. Long data records

410　(exceeding 10 years) are available from some of these sites, in Europe (e.g. Lindenberg (GER),

411　Payerne (SUI), and Potenza (IT)) as well as in the USA (e.g. ARM sites; Cadeddu et al. 2013).

412　MWR data assimilation promises to be useful for adjusting NWP model temperature and

413　humidity fields of the lowest 2 km, especially in convective (Cimini et al. 2015) and very stable

414　conditions (Martinet et al. 2017).　Fig. 8 shows how the assimilation of MWR brightness

415　temperatures leads to an improvement in the temperature analysis in an enclosed Alpine valley

416　during stable conditions where the true structure has been established from a series of

417　radiosonde ascents; the stability close to the ground is a crucial parameter in the build-up and

418   dispersion of pollutants. Similarly, Fig. 9 shows large potential improvements in both

419   temperature and humidity profiles when observations from one MWR are used to correct the

420   NWP forecast, in a so-called one-dimensional variational retrieval (1DVAR) scheme. 24-hour

421   time series of temperature and humidity profiles from a NWP forecast, 1DVAR retrievals, and

422   the analysis increment are shown. Based on these results, Météo-France decided to deploy a

423   MWR network for an international fog field campaign planned for Dec 2019-Feb 2020 (four

424   to six MWR units in a 300x200 km domain). Forecast indices derived from MWR observations

425   were also demonstrated to be useful in support of nowcasting and short-range weather

426   forecasting (Cimini et al. 2015). Continental-scale data assimilation trials show positive-to-

427   neutral impact, especially for accumulations of precipitation up to 18h after forecast

428   initialization (Caumont et al. 2016). The impact of MWR-derived thermodynamic profiles is

429   larger when they are used to substitute classical radiosonde observations in a data denial

430   experiment. Data assimilation results obtained so far did not take advantage of the recent

431   hardware and software developments, so there is clearly potential for improvement.

432

433   **CONCLUSIONS**

434   Networks of ground-based profiling instruments with improved retrieval algorithms and

435   standardized software and calibration procedures have been developed by TOPROF in

436   collaboration with instrument manufacturers and implemented by the E-PROFILE program of

437   the EUMETNET consortium of European National Weather Services. These networks are

438   providing an increased understanding of process within the lowest few km of the atmosphere,

439   and, ultimately, have the potential for assimilation into operational NWP models.

440   Improvements have been made in the Automatic Lidar and Ceilometer (ALC) algorithms that

441   correct for overlap, remove artifacts in the profiles, and provide absolute backscatter calibration

442   to within ~10% using natural targets as a reference; either the integrated backscatter from thick

443   water clouds or the molecular return. The network has the demonstrated capability for tracking

444   smoke from forest fires and desert dust, issuing fog formation warnings, and for providing

445   vertical profiles of cloud and aerosols. An O-B comparison of the observed backscatter from

446   desert dust with those from an ECMWF forward model indicates that biases are below 10%.

447   Profiles of aerosol and cloud backscatter from a network of 220 ALCs (as of September 2018)

448   are being distributed in real time to European weather forecast centers and this should increase

449   to several hundreds within the next year.

450

451   A network of Doppler Wind Lidars (DWLs) is being set up and test data are now being

452   distributed in experimental mode to forecast centers by E-PROFILE. DWLs use aerosol or

453   cloud particles as tracers of the line of sight component of atmospheric motion. Standardized

454   scanning procedures and algorithms have been established so they can routinely provide data

455   on wind profiles in the boundary layer with an rms accuracy of $< 10°$ in direction and better

456   than 0.7 m s^{-1} in speed. These observations can be used for diagnosis of the existence of low-

457   level jets, deriving profiles of vertical velocity variance and skewness, and the dissipation rate

458   of turbulent kinetic energy. The combination of the wind and turbulence can be used to

459   diagnose wind gusts, needed for forecasting and assessing wind-induced damage, and for

460   classification of the atmospheric boundary layer structure so that those turbulent layers in

461   contact with the surface can be identified; this is an important property when calculating the

462   dispersion by chemical transport models.

463

464   TOPROF studies have led to advances in Microwave Radiometer (MWR) hardware and

465   software so the instruments can provide brightness temperature (T_B) calibrations to within

466   0.1K. A ground-based version of the RTTOV radiative transport model has been developed

467   and characterized, so that T_B and its uncertainty can be calculated from a forecast model. Tests

468   over one year comparing these forward modeled values of T_B with those observed with a

469   prototype network of six MWRs show that typical O-B biases for well-maintained instruments

470   are generally below 1K. Field campaigns have demonstrated that the assimilation of T_B into an

471   operational mesoscale model leads to improved temperature and humidity structure in the

472   lowest 2 km of the atmosphere. E-PROFILE is evaluating the extension of their activities to

473   MWR so that data can be distributed in real time to European weather forecast centers starting

474   from 2019.

475

479

480   **REFERENCES**

481   Baars, H. and Coauthors, 2016: An overview of the first decade of Polly[NET]: an emerging

482   network of automated Raman-polarization lidars for continuous aerosol profiling. *Atmos.*

483   *Chem. Phys.*, **16**, 5111-5137. doi:10.5194/acp-16-5111-2016.

484   Benedetti, A. and Coauthors, 2009: Aerosol analysis and forecast in the European Centre for

485   Medium-Range Weather Forecasts Integrated Forecast System: 2. Data assimilation. *J.*

486   *Geophys. Res.,* **141** D13205. doi:10.1029/2008JD011115.

487   Cadeddu, M. P., Liljegren, J. C., and Turner, D. D., 2013: The Atmospheric radiation

488   measurement (ARM) program network of microwave radiometers: instrumentation, data,

489   and retrievals. *Atmos. Meas. Tech.*, **6**, 2359–2372, https://doi.org/10.5194/amt-6- 2359-

490   2013.

491   Caumont O., D., and Coauthors 2016: Assimilation of humidity and temperature observations

492   retrieved from ground-based microwave radiometers into a convective-scale model. *Q. J. R.*

493   *Meteorol. Soc.,* **142**: 2692–2704. doi:10.1002/qj.2860.

494   Cazorla, A., and Coauthors, 2017: Near-real-time processing of a ceilometer network assisted

495   with sun-photometer data: monitoring a dust outbreak over the Iberian Peninsula. *Atmos.*

496   *Chem. Phys.*, **17**, 11861–11876. https://doi.org/10.5194/acp-17-11861-2017.

497   Chan, K. L., and Coauthors, 2018: Evaluation of ECMWF-IFS (version 41R1) operational

498   model forecasts of aerosol transport by using ceilometer network measurements. *Geosci.*

499   *Model. Dev.*, **11**, 3807-3831. doi.org/10.5194/gmd-11-3807-2018.

500   Cimini, D., M. Nelson, J. Güldner, and R. Ware, 2015: Forecast indices from a ground-based

501   microwave radiometer for operational meteorology. *Atmos. Meas. Tech.*, **8**, 315-333,

502   https://doi.org/10.5194/amt-8-315-2015.

503   Cimini, D., and Coauthors, 2018: Uncertainty of atmospheric microwave absorption model:

504   impact on ground-based radiometer simulations and retrievals. *Atmos. Chem. Phys.*

505   *Discuss.*, https://doi.org/10.5194/acp-2018-536. In review.

506   De Angelis, F., and Coauthors, 2016: RTTOV-gb – adapting the fast radiative transfer model

507   RTTOV for the assimilation of ground-based microwave radiometer observations. *Geosci.*

508   *Model Dev.*, **9**, 2721–2739, https://doi.org/10.5194/gmd-9-2721-2016.

509   De Angelis, F., and Coauthors, 2017: Long-term observations minus background monitoring

510   of ground-based brightness temperatures from a microwave radiometer network. *Atmos.*

511   *Meas. Tech.*, **10**, 3947-3961, https://doi.org/10.5194/amt-10-3947-2017.

512   Fernald, F. G., B. M. Herman, and J. A. Reagan, 1972: Determination of Aerosol Height

513   Distributions by Lidar, *J. Appl. Meteorol.*, **11,** 482–489, doi:10.1175/1520-

514   0450(1972)011<0482:DOAHDB>2.0.CO;2.

515   Gryning, S.E., and Coauthors, 2016: Weibull wind-speed distribution parameters derived from

516   a combination of wind-lidar and tall-mast measurements over land, coastal and marine sites.

517   *Boundary-Layer Meteorol*., **159**, 329–348, doi:10.1007/s10546-015-0113-x.

518   Haeffelin, M., and Coauthors, 2012: Evaluation of mixing height retrievals from automatic

519   profiling lidars and ceilometers in view of future integrated networks in Europe. *Boundary-*

520   *Layer Meteorol.,* **143**, 49–75.

521   Haeffelin, M., and Coauthors, 2016: Radiation fog formation alerts using attenuated

522   backscatter power from automatic Lidars and ceilometers. *Atmos. Meas. Tech*., **9**, 5347-

523   5365.

524   Hervo, M., Y. Poltera, and A. Haefele, 2016: An empirical method to correct for temperature-

525   dependent variations in the overlap function of CHM15k ceilometers. *Atmos. Meas. Tech.*,

526   **9**, 2947–2959, doi:10.5194/amt-9-2947-2016.

527   Hopkin, E, and Coauthors, 2018: A robust automated technique for operational calibration of

528   ceilometers using the integrated backscatter from totally attenuating liquid clouds.

529   Submitted to *Atmos. Meas. Tech.*

530   Illingworth, A. J., and Coauthors, 2007: Cloudnet: Continuous evaluation of cloud profiles in

531   seven operational models using ground-based observations. *Bull. Amer. Meteor. Soc.*, **88**,

532   883–898, doi:10.1175/BAMS-88-6-883.

533   Illingworth, A. J., and Coauthors, 2015: Exploiting Existing Ground-Based Remote Sensing

534   Networks to Improve High-Resolution Weather Forecasts. *Bull. Amer. Meteor. Soc.*, **96**,

535   2107-2125, doi:10.1175/BAMS-D-13-00283.1

536   Klett, J. D., 1985: Lidar Inversion with Variable Backscatter Extinction Ratios. *Appl. Opt*., **24**,

537   1638–1643, doi: 10.1364/AO.24.001638.

538   Kotthaus, S. and C. S. B. Grimmond, 2018: Atmospheric Boundary Layer Characteristics from

539   Ceilometer measurements Part 1: A new method to track mixed layer height and classify

540   clouds. *Q. J. R. Meteorol. Soc.*, in press, doi:10.1002/qj.3299.

541   Kotthaus, S., and Coauthors, 2016: Recommendations for processing atmospheric attenuated

542   backscatter profiles from Vaisala CL31 ceilometers. *Atmos. Meas. Tech.,* **9**, 3769–3791,

543   doi:10.5194/amt-9-3769-2016.

544   Lotteraner, C., and M. Piringer, 2016: Mixing-height time series from operational ceilometer aerosol-

545   layer heights. *Boundary-Layer Meteorology*, **161**, 265-287

546   Manninen A. J., O'Connor, E. J., Vakkari, V. and T. Petäjä, 2016: A generalised background

547   correction algorithm for a Halo Doppler lidar and its application to data from Finland.

548   *Atmos. Meas. Tech.*, **9**, 817–827, doi:10.5194/amt-9-817-2016.

549   Manninen A. J., T. Marke, M. Tuononen, and E. J. O'Connor, 2018: Atmospheric boundary

550   layer classification with Doppler lidar. *J. Geophys. Res*., Accepted for publication.

551   doi: 10.1029/2017jd028169.

552   Marke, T., and Coauthors, 2018: Long-Term Observations and High-Resolution Modeling of

553   Midlatitude Nocturnal Boundary Layer Processes Connected to Low-Level Jets. *J. Appl.*

554   *Meteor. Climatol.,* **57**, 1155–1170, https://doi.org/10.1175/JAMC-D-17-0341.1.

555   Martinet, P., D. and Coauthors, 2017: Combining ground-based microwave radiometer and the

556   AROME convective scale model through 1DVAR retrievals in complex terrain: an Alpine

557   valley case study. *Atmos. Meas. Tech.*, **10**, 3385-3402. https://doi.org/10.5194/amt-10-

558   3385-2017.

559   O'Connor, E. J., A. J. Illingworth, and R. J. Hogan, 2004: A technique for autocalibration of

560   cloud lidar. *J. Atmos. Ocean. Technol*., **21**, 777–786.

561   EJ O'Connor, E.J. and Coauthors, 2010: A method for estimating the turbulent kinetic energy

562   dissipation rate from a vertically-pointing Doppler lidar, and independent evaluation from

563   balloon-borne in-situ measurements. *J. Ocean and Atmos Tech.,* **27**, 1652-1664.

564   Päschke, E., R. Leinweber, and V. Lehmann, 2015: An assessment of the performance of a 1.5

565   μm Doppler lidar for operational vertical wind profiling based on a 1-year trial. *Atmos.*

566   *Meas. Tech.*, **8**, 2251-2266. https://doi.org/10.5194/amt-8-2251-2015.

567   Pattantyús-Ábrahám, M., and Coauthors, 2017: The Dataset of the CeiLinEx 2015 Ceilometer-

568   Inter-comparison Experiment, Version v001, doi 10.5676/DWD/CEILINEX2015.

569   Poltera, Y., and Coauthors, 2017: Pathfinder TURB: an automatic boundary layer algorithm.

570   Development, validation and application to study the impact on in-situ measurements at the

571   Jungfraujoch.   *Atmos.   Chem.   Phys.*,   **17**,   10051-10070.

572   https://doi.org/10.5194/acp-17-10051-2017.

573   Román, R., and Coauthors, 2018: Retrieval of aerosol profiles combining sun-photometer and

574   ceilometer measurements in GRASP code. *Atmospheric Research*, **204**, 161-177.

575   Rottner, L., C. Baehr, A. Dabas and L. Hammoud, 2017: Stochastic method for turbulence

576   estimation from Doppler lidar measurements. *Journal of Applied Remote Sensing* **11**(4),

577   046001. doi:10.1117/1.JRS.11.046001.

578   Rose, T., S. Crewell, U. Löhnert, and C. Simmer, 2005: A network suitable microwave

579   radiometer for operational monitoring of the cloudy atmosphere. *Atmos. Res.*, **75**, 183–

580   200, https://doi.org/10.1016/j.atmosres.2004.12.005.

581   Seity, Y., and Coauthors, 2011: The AROME-France convective- scale operational model,

582   *Mon. Weather Rev.*, **139**, 976–991.

583   Schween, J. H., A. Hirsikko, U. Löhnert, and S. Crewell, 2014: Mixing layer height retrieval

584   with ceilometer and Doppler lidar: from case studies to long-term assessment. *Atmos. Meas.*

585   *Tech.*, **7,** 3685-3704. http://dx.doi.org/10.5194/amt-7-3685-2014.

586 Suomi, I., S.-E. Gryning, E. J. O'Connor, and T. Vihma, 2017: Methodology for obtaining wind

587   gusts using Doppler lidar. *Q.J.R. Meteorol. Soc.*, **143**: 2061–2072. doi:10.1002/qj.3059.

588 Teschke, G. and V. Lehmann, 2017: Mean wind vector estimation using the velocity–azimuth

589   display (VAD) method: an explicit algebraic solution. *Atmos. Meas. Tech.*, **10**, 3265-3271.

590   https://doi.org/10.5194/amt-10-3265-2017.

591 Tuononen, M., E.J. O'Connor, V.A. Sinclair, and V. Vakkari, 2017: Low-Level Jets over Utö,

592   Finland, Based on Doppler Lidar Observations. *J. Appl. Meteor. Climatol.*, **56**, 2577–2594.

593   https://doi.org/10.1175/JAMC-D-16-0411.1.

594 Vakkari, V., E. J. O'Connor, A. Nisantzi, R. E. Mamouri, and D. G. Hadjimitsis, 2015: Low-

595   level mixing height detection in coastal locations with a scanning Doppler lidar. *Atmos.*

596   *Meas. Tech.*, **8**, 1875-1885. doi:10.5194/amt-8-1875-2015.

597 Ware, R., and Coauthors, 2003: A multichannel radiometric profiler of temperature,

598   humidity, and cloud liquid. *Radio Sci.*, **38**, 8079, https://doi.org/10.1029/2002RS002856,

599   2003.

600 Warren, E., and Coauthors, 2018: Evaluation of forward-modelled attenuated backscatter

601   using an urban ceilometer network in London under clear-sky conditions. *Atmos. Environ.*,

602   **191,** 532-547. doi:https://doi.org/10.1016/j.atmosenv.2018.04.045.

603 Westbrook, C. D., A. J. Illingworth, E. J. O'Connor, and R. J. Hogan, 2010: Doppler lidar

604   measurements of oriented planar ice crystals falling from supercooled and glaciated cloud

605   layers. *Q. J. R. Meteorol. Soc.*, **136**, 260–276. doi:10.1002/qj.528.

606 Wiegner, M. and A. Geiß, 2012: Aerosol profiling with the Jenoptik ceilometer CHM15kx.

607   *Atmos. Meas. Tech.*, **5**, 1953–1964. doi:10.5194/amt-5-1953-2012.

608 Wiegner, M., and Coauthors, 2014: What is the benefit of ceilometers for aerosol remote

609   sensing? An answer from EARLINET. *Atmos. Meas. Tech.,* **7**, 1979-1997,

610   https://doi.org/10.5194/amt-7-1979-2014.

611 Wiegner, M and J. Gasteiger. 2015: Correction of water vapor absorption for aerosol remote

612   sensing with ceilometers. *Atmos. Meas. Tech.*, **8,** 3971–3984. doi:10.5194/amt-8-3971-

613   2015.

614

615 **SIDEBAR: THE TOPROF COST ACTION**

616 COST or 'European Cooperation in Science and Technology' is a European Union funded

617 program that enables researchers to set up an interdisciplinary research networks in Europe and

618 beyond. Twenty-two European countries participated in the TOPROF action with researchers

619 from 16 National Weather Services attending together with representatives from six European

620 manufacturers of ALCs, DWLs and MWRs. Three day meetings were held twice a year each

621 with about 50 participants, but most importantly TOPROF supported 24 separate week long

622 visits by individual scientists to other research labs, national weather services, or industry,

623 where they tackled specific problems such as: changes to calibration procedures, modifications

624 to data processing that resulted in new public releases of software, physical modification of the

625 instruments and testing of forward models at national weather services. In addition, there were

626 12 special meetings to plan, execute and discuss field projects dedicated to comparing the

627 performance of different instruments with various configurations, and in some cases with

628 independent validation using instrumented towers and/or special radiosonde ascents.

629

630 **FIGURE CAPTIONS**

631 **Fig. 1.** Map of the ALC network (green - operational E-PROFILE stations: blue - stations

632 planned for 2018: red - other ceilometers reported by DWDs ceilomap). Example of E-

633 PROFILE measurements during the Saddleworth Moor fire near Manchester (26 to 27 June

634 2018). Five stations are represented: Stornoway, Eskdalemuir, Flesland, Rotterdam and

635 Ulrichstein. A photograph of the fire (courtesy E. J. O'Connor) is shown in the lower left

636 corner.

637

638 **Fig 2**. The 1064 nm attenuated backscatter for a frontal passage over Ulm, Germany on 25

639 August 2018 measured by a CHM15k ceilometer. Clouds and rain appear in black, red and

640 orange colors. Areas in green, yellow, and orange are aerosol layers. Areas above clouds where

641 the ceilometer signal is extinguished are plotted in white.

642

643 **Fig 3.** ALC measurements from eight co-located ALCs including Campbell Scientific, Vaisala,

644 and Lufft instruments based on 3 hours of data on 13 Aug 2015 during the Ceilinex campaign

645 in Lindenberg, Germany. (Left panel) raw instrument signal; (Right panel) calibrated

646 attenuated backscatter signal. $1\,Mm = 10^6\,m$. Note the increased noise for the CL31 above 2km

647 and the divergence of the profiles below 500 m.

648

649 **Fig. 4.** Upper left panel: Attenuated Backscatter measured by the CHM15k in Valladolid

650 during a Saharan dust event from 20 to 27 June 2018. Data above clouds and with SNR lower

651 than 3 are removed. Lower left panel: Attenuated Backscatter forecast by CAMS model at the

652 closest grid point. Upper right panel: Median attenuated backscatter measured (in red) and

653 forecast (in black). Lower right panel: median of the bias between observations and forecasts.

654 Shading represents 25th and 75th percentiles.

655

656 **Fig. 5.** Three-hour time series plot generated automatically from measurements taken at

657 Charles-de-Gaulle airport (France) on 21 Jan 2016. (Top panel): fog alerts based on the method

658 of Haeffelin et al. (2016). (Lower panel): 0-400m ALC attenuated backscatter profile ($m^{-1}\,sr^{-1}$,

659 shown on a colored log scale) and horizontal visibility close to the surface (m, shown as a

660 gray line, the vertical axis shows the visibility on a log scale). The 1-km horizontal-visibility

661   threshold, adopted by WMO to define fog, is shown as a gray dashed line. Plots generated in

662   real-time are available at: http://www.lmd.polytechnique.fr/~sirta/parafog/.

663

664   **Fig. 6.** 24-hour time-height plots of Doppler lidar products generated from a Halo Photonics

665   Streamline operating in Helsinki, Finland, on 24 March 2014: (a) attenuated backscatter

666   coefficient, (b) wind speed including objective low-level jet diagnosis (black circles), (c) wind

667   direction, (d) dissipation rate of turbulent kinetic energy. The wind profiles are obtained from

668   scans at two elevations, 15 and 70 degrees from horizontal. Helsinki is situated on a coast line

669   that is aligned approximately east-west and the Doppler lidar is located about 6 km inland from

670   the coast. This combination of products illustrates the complexity of the boundary layer in a

671   coastal and urban environment, with a sea breeze driving a marine boundary layer inland

672   (northerly low-level flow from sea to land) underneath a much deeper land boundary layer

673   (more southerly flow from land to sea aloft). Solar noon is around 10 UTC, and after 1900

674   UTC all flow is from land to sea.

675

676   **Fig. 7.** One-year time series of the O–B T_B differences at Jülich (adapted from De Angelis et

677   al. 2017). From top to bottom: channels 22.24 (blue), 31.40 (red), 52.28 (magenta), and 58.00

678   GHz (cyan). Typically, RMS at zenith are within 3 K with low bias; for instrument, channel,

679   and observing angle dependencies see De Angelis et al. (2017). The black circle indicates the

680   date of a new liquid nitrogen calibration. Were such a monitoring available operationally, the

681   faulty calibration could have been detected earlier and the recalibration could have been

682   validated in near-real-time. The NWP model used here is AROME, Application of Research

683   to Operations at Mesoscale, developed by Météo-France (Seity et al., 2011).

684

685   **Fig. 8.** Profiles of RMSE with respect to radiosonde observations of the AROME NWP model

686   background (dashed) and 1DVAR updated analysis (solid) in clear (left) and cloudy (right) sky

687   conditions. During stable conditions in an enclosed alpine valley, 1DVAR assimilation of

688   MWR brightness temperatures lead to an improvement in the temperature analysis in the first

689   1500 m up to 7.5 K in clear conditions and up to ~4 K in cloudy conditions. Data from the

690   Passy-2015 field campaign (December 2014 to March 2015), Arve River valley near Passy,

691   France (Martinet et al., 2017).

692

693   **Fig. 9.** 24-hour time series (28 October 2016) of temperature (top) and humidity (bottom) from

694   AROME NWP model (left), 1DVAR analysis update (center), and the difference between the

695   two (right) showing temperature increments of up to 5 K. Data from a fog field campaign at

696   Observatoire Perenne de l'Environnement (Lat: 48.56; Lon: 5.50; Alt: 388 m) near Bure

697   (France). The campaign extended from Sep 2015 to Apr 2016 and included one MWR unit.

698   NWP system is AROME 1h forecast cycle, 1.3 km horizontal resolution, 90 vertical levels.

699   The nearest grid-point 1-hour forecast is used as background for the 1DVAR retrievals at 1-

700   hour resolution, based on the closest measurements within 15 minutes.

701

702

703

704

Fig. 1. Map of the ALC network (green - operational E-PROFILE stations: blue - stations planned for 2018: red - other ceilometers reported by DWDs ceilomap). Example of E-PROFILE measurements during the Saddleworth Moor fire near Manchester (26 to 27 June 2018). Five stations are represented: Stornoway, Eskdalemuir, Flesland, Rotterdam and Ulrichstein. A photograph of the fire (courtesy E. J. O'Connor) is shown in the lower left corner.

Fig 2. The 1064 nm attenuated backscatter for a frontal passage over Ulm, Germany on 25 August 2018 measured by a CHM15k ceilometer. Clouds and rain appear in black, red and orange colors. Areas in green, yellow, and orange are aerosol layers. Areas above clouds where the ceilometer signal is extinguished are plotted in white.

729

730

731 **Fig. 3** ALC measurements from eight co-located ALCs including Campbell Scientific, Vaisala,

732 and Lufft instruments based on 3 hours of data on 13 Aug 2015 during the Ceilinex campaign

733 in Lindenberg, Germany. (Left panel) raw instrument signal; (Right panel) calibrated

734 attenuated backscatter signal. 1 Mm = 10^6 m. Note the increased noise for the CL31 above 2km

735 and the divergence of the profiles below 500 m.

736

737

738
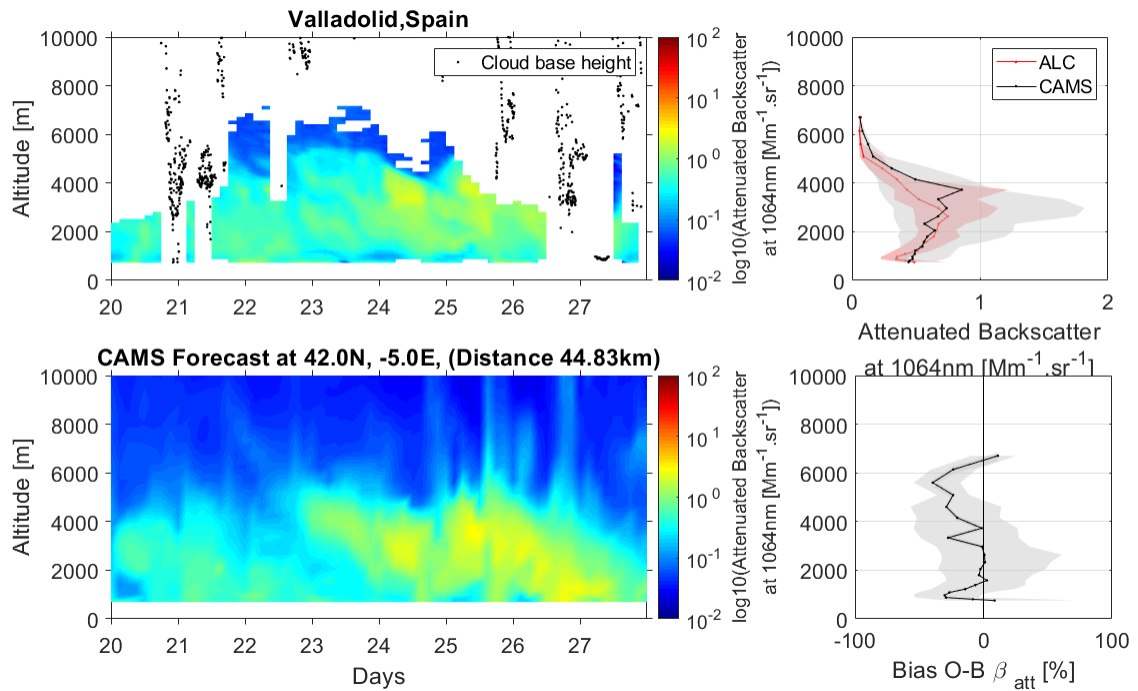
Fig. 4. Upper left panel: Attenuated Backscatter measured by the CHM15k in Valladolid during a Saharan dust event from 20 to 27 June 2018. Data above clouds and with SNR lower than 3 are removed. Lower left panel: Attenuated Backscatter forecast by CAMS model at the closest grid point. Upper right panel: Median attenuated backscatter measured (in red) and forecast (in black). Lower right panel: median of the bias between observations and forecasts. Shading represents 25th and 75th percentiles
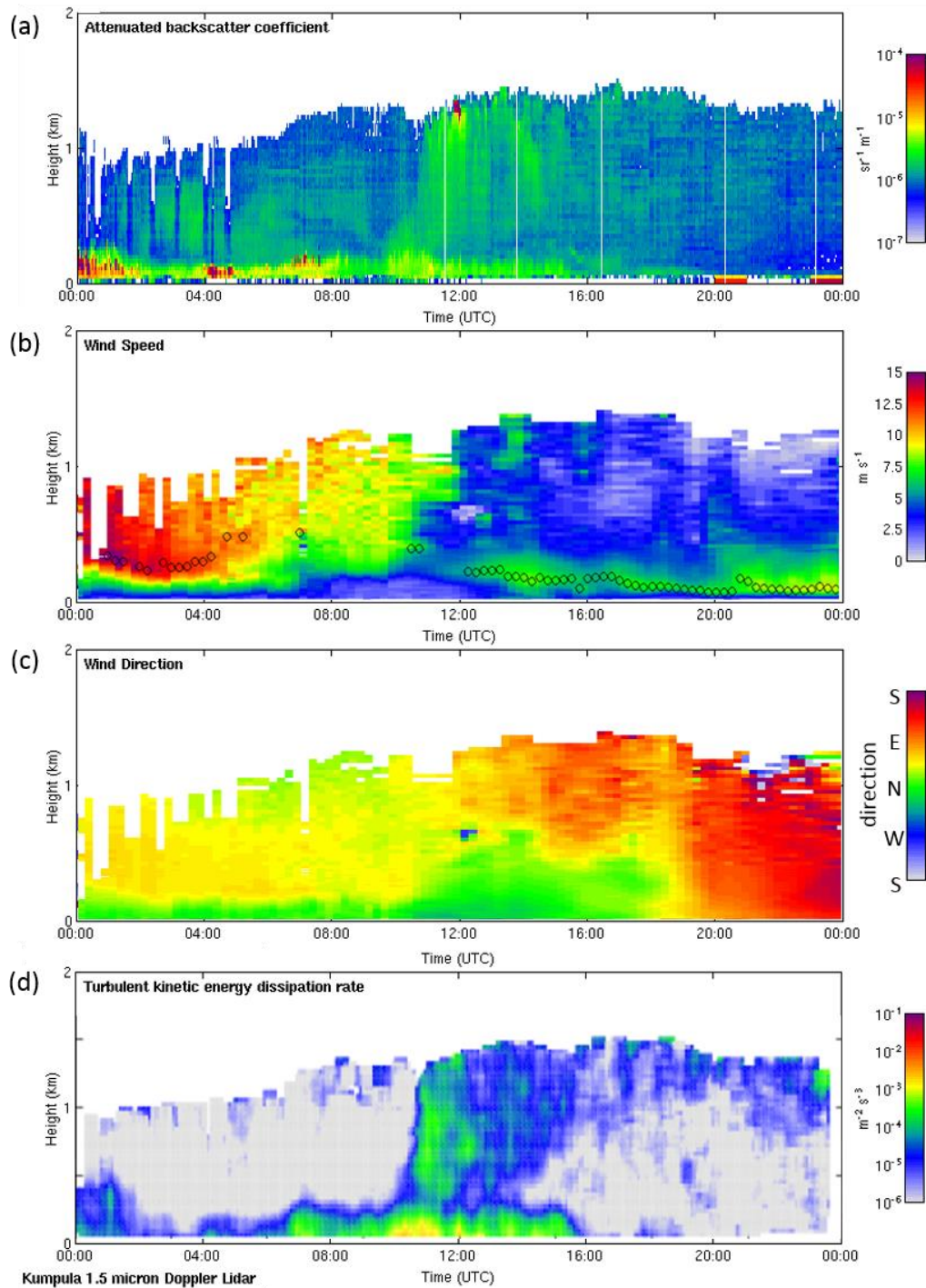
Fig. 5. Three-hour time series plot generated automatically from measurements taken at Charles-de-Gaulle airport (France) on 21 Jan 2016. (Top panel): fog alerts based on the method of Haeffelin et al. (2016). (Lower panel): 0-400 m ALC attenuated backscatter profile (m^{-1} sr^{-1}, shown on a colored log scale) and horizontal visibility close to the surface (m, shown as a gray line, the vertical axis shows the visibility on a log scale). The 1-km horizontal-visibility threshold, adopted by WMO to define fog, is shown as a gray dashed line. Plots generated in real-time are available at: http://www.lmd.polytechnique.fr/~sirta/parafog/.

763
764
765 **Fig. 6.** 24-hour time-height plots of Doppler lidar products generated from a Halo Photonics

766 Streamline operating in Helsinki, Finland, on 24 March 2014: (a) attenuated backscatter

767 coefficient, (b) wind speed including objective low level jet diagnosis (black circles), (c) wind

768 direction, (d) dissipation rate of turbulent kinetic energy. The wind profiles are obtained from

769 scans at two elevations, 15 and 70 degrees from horizontal. Helsinki is situated on a coast line

770   that is aligned approximately east-west and the Doppler lidar is located about 6 km inland from

771   the coast. This combination of products illustrates the complexity of the boundary layer in a

772   coastal and urban environment, with a sea breeze driving a marine boundary layer inland

773   (northerly low-level flow from sea to land) underneath a much deeper land boundary layer

774   (more southerly flow from land to sea aloft). Solar noon is around 10 UTC, and after 1900

775   UTC all flow is from land to sea.

776
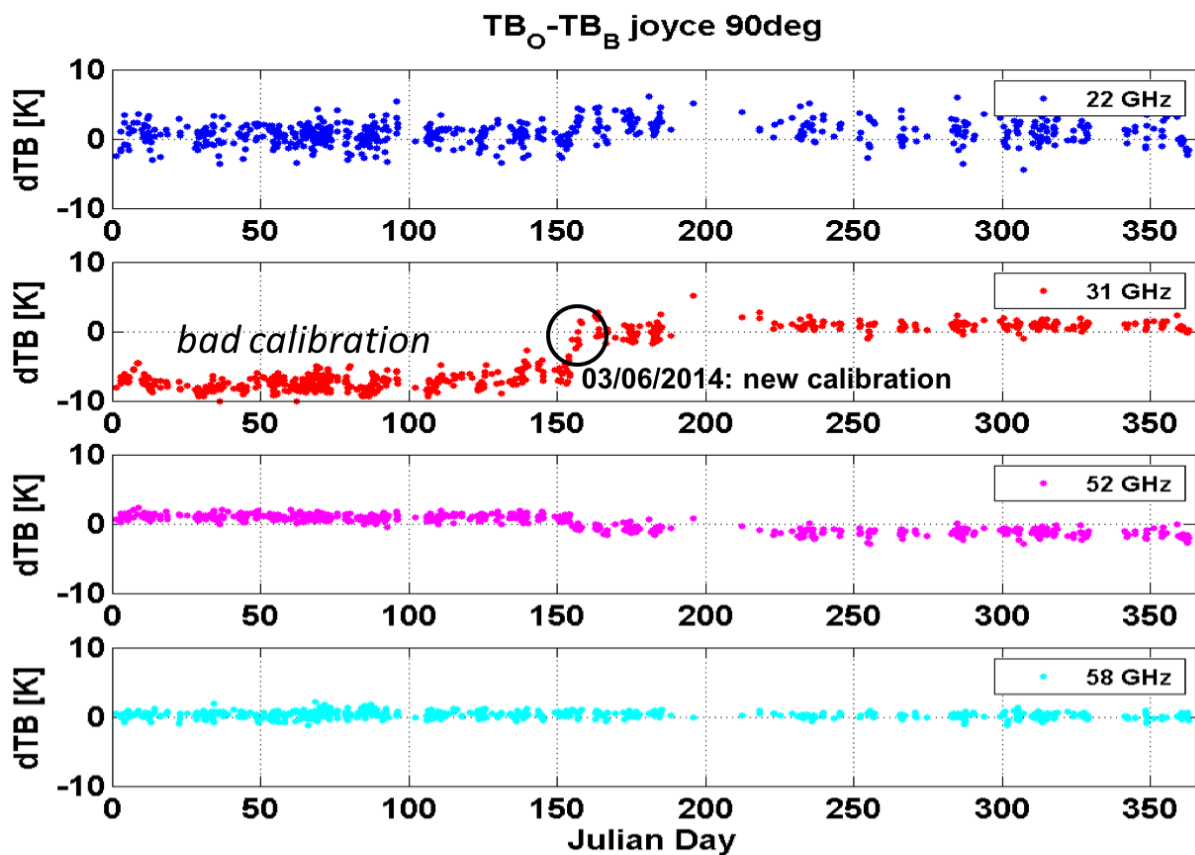
777
778

779   **Fig. 7**. One-year time series of the O–B T_B differences at Jülich (adapted from De Angelis et

780   al. 2017). From top to bottom: channels 22.24 (blue), 31.40 (red), 52.28 (magenta), and 58.00

781   GHz (cyan). Typically, RMS at zenith are within 3 K with low bias; for instrument, channel,

782   and observing angle dependencies see De Angelis et al. (2017). The black circle indicates the

783   date of a new liquid nitrogen calibration. Were such a monitoring available operationally, the

784   faulty calibration could have been detected earlier and the recalibration could have been

785 validated in near-real-time. The NWP model used here is AROME, Application of Research to

786 Operations at Mesoscale, developed by Météo-France (Seity et al., 2011).

787

788
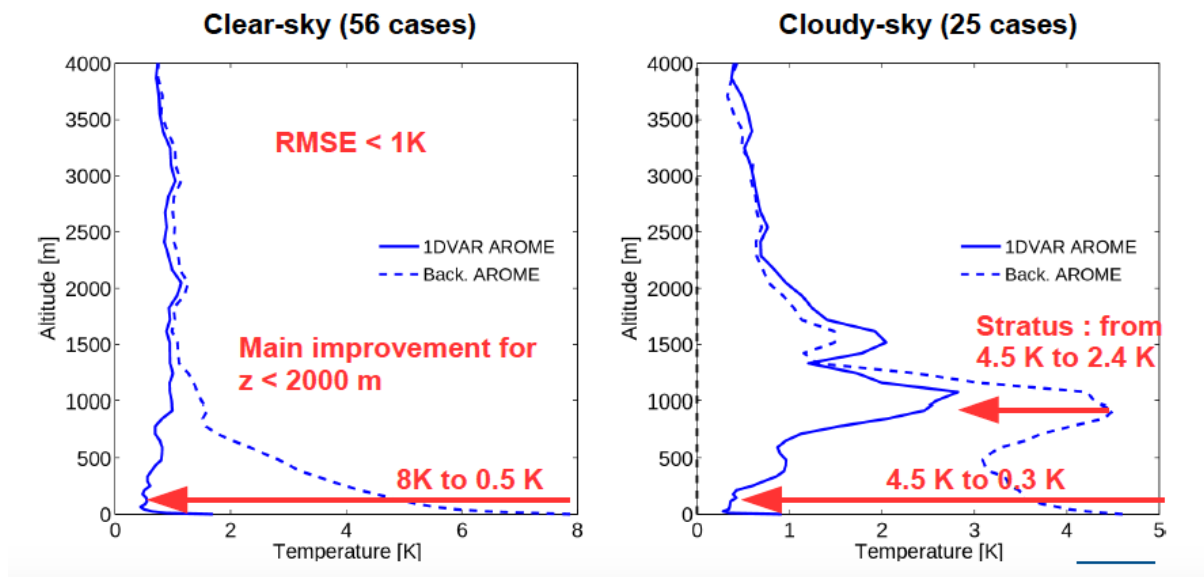
789

790

791 **Fig. 8.** Profiles of RMSE with respect to radiosonde observations of the AROME NWP model
792 background (dashed) and 1DVAR updated analysis (solid) in clear (left) and cloudy (right) sky
793 conditions. During stable conditions in an enclosed alpine valley, 1DVAR assimilation of
794 MWR brightness temperatures lead to an improvement in the temperature analysis in the first
795 1500 m up to 7.5 K in clear conditions and up to ~4 K in cloudy conditions. Data from the
796 Passy-2015 field campaign (December 2014 to March 2015), Arve River valley near Passy,
797 France (Martinet et al., 2017).

798

799

800
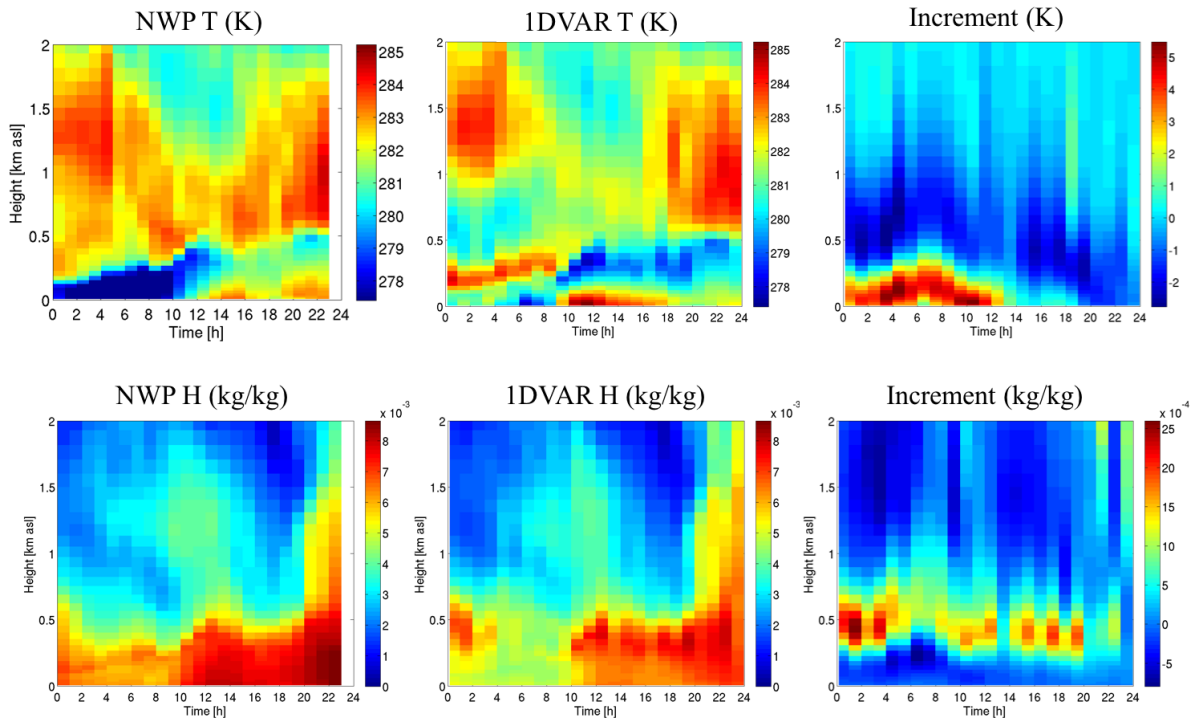
Fig. 9. 24-hour time series (28 October 2016) of temperature (top) and humidity (bottom) from AROME NWP model (left), 1DVAR analysis update (center), and the difference between the two (right) showing temperature increments of up to 5 K. Data from a fog field campaign at Observatoire Perenne de l'Environnement (Lat: 48.56; Lon: 5.50; Alt: 388 m) near Bure (France). The campaign extended from Sep 2015 to Apr 2016 and included one MWR unit. NWP system is AROME 1h forecast cycle, 1.3 km horizontal resolution, 90 vertical levels. The nearest grid-point 1-hour forecast is used as background for the 1DVAR retrievals at 1-hour resolution, based on the closest measurements within 15 minutes.